Material characterization and finite element modelling of cyclic plasticity behavior for 304 stainless steel using a crystal plasticity model

Jiawa Lu[a*], Wei Sun[a], Adib Becker[a]

[a] *Department of Mechanical, Materials and Manufacture Engineering, The University of Nottingham, University Park, Nottingham, NG7 2RD, UK*

*Corresponding Author Email: eaxjl2@nottingham.ac.uk

Abstract: Low cycle fatigue tests were carried out for a 304 stainless steel at room temperature. A series of experimental characterisations, including SEM, TEM, and XRD were conducted on for the 304 stainless steel to facilitate the understanding of the mechanical responses and microstructural behaviour of the material under cyclic loading including nanostructure, crystal structure and the fractured surface. The crystal plasticity finite element method (CPFEM) is a powerful tool for studying the microstructure influence on the cyclic plasticity behaviour. This method was incorporated into the commercially available software ABAQUS by coding a UMAT user subroutine. Based on the results of fatigue tests and material characterisation, the full set of material constants for the crystal plasticity model was determined. The CPFEM framework used in this paper can be used to predict the crack initiation sites based on the local accumulated plastic deformation and local plastic dissipation energy criterion, but with limitation in predicting the crack initiation caused by precipitates.

Keywords: Material characterisation; Cyclic plasticity; Finite element method; 304 stainless steel

Nomenclature

$\boldsymbol{L}$	Velocity gradient	V	Volume	γ	Shear strain
$\boldsymbol{F}$	Deformation gradient	G	Shear Modulus	τ	Shear stress
$\boldsymbol{\sigma}$	Stress	b	Burger's vector	g	Critical shear stress
$\boldsymbol{\varepsilon}$	Strain	Δ	Range	χ	Backstress
$\boldsymbol{m}$	Slip direction	*	Lattice deformation	ρ	Dislocation density
$\boldsymbol{n}$	Slip normal	p	Plastic deformation	α, β	Index of slip system
$\boldsymbol{D}$	Deformation tensor	$\boldsymbol{\Omega}$	Rotational tensor	$\boldsymbol{\mu}$	Schmid factor
$\boldsymbol{R}$	Rotation matrix	2θ	Bragg angle	y_c	Critical annihilation length
$\boldsymbol{\omega}$	Lattice spin tensor		Cij	2^{nd} order elastic moduli matrix	
$\boldsymbol{A}$	Dislocation interaction matrix		$\mathcal{L}_{ijkl}$	4^{th} order elastic moduli tensor	

1 Introduction

304 stainless steel is a type of austenitic steel widely used in pipes of chemical plants and many other applications which may be subject to cyclic loading conditions. The predictions of fatigue life and crack initiation sites are important aspects of designing the plant structure. Fatigue failure is usually caused by the creation of microcracks smaller than the grain size, then the growth and coalescence of micro flaws to a dominant crack, followed by stable propagation of the dominant macrocrack, and structural instability or complete fracture finally.

Microcrack nucleation is influenced by a range of mechanical, microstructural and environmental factors. Dunne [1] investigated the microcrack initiation and propagation for FCC nickel-based super-alloy phenomenon. It was found by experimental observation that fatigue induced microcracks smaller than the grain size could initiate at multiple locations, including grain boundaries, precipitates, PSBs, and surface inclusions and extrusions. These microcracks grow by coalescence to form a dominant crack, which is influenced strongly by the grain orientation. In addition, not all microcracks would propagate, and the slip propagation direction is parallel with the active slip direction within the grain. It was further pointed out by Bhat [2] that the crack initiation sites depend on the applied loading. For high cycle fatigue when the strain amplitude is low, strain tends to be localised at persistent slip bands and this is where the crack initiates. On the contrary, for low cycle fatigue when the strain amplitude is high, the grain boundary becomes the crack initiation site, since dislocations pile up at the grain boundary. For the intermediate strain amplitude, damage initiates on both grain boundary and slip traces. It is also concluded by Hanlon [3, 4] that fatigue crack initiation sites depend on the grain size and grain size arrangement. Crack initiation is favoured in a corase-grain material compared to a fine grain material. Grain refinement increases the fatigue limit, while reducing the microcrack initiation threshold, but it also increases the fatigue crack growth rate. Based on a study on waspaloy[5, 6], it was also pointed out that the crack initiation sites tend to be larger than the average grain size, but not necessarily the largest grain size. The crack initiation grains normally are located within some cluster of grains with misorientations less than 15^{o}, which act similar to a large single grain.

The crystal plasticity method is a systematic method which relates the microscale material properties, relating to grain and morphology, to the mesoscale mechanical behavior. The pioneering work of the crystal plasticity method was performed by Taylor [7] for face cubic centered (FCC) polycrystals subject to large plastic strains, in which it was assumed that the strain in each grain was homogeneous and equal to the macroscopic polycrystalline strain. In addition, it was proposed that at least five slip systems should be available for the plastic deformation, and the minimum work principle was used to determine the five active slip systems. This model is quite limited in application since this transition model linking the local to the bulk material behaviour did not consider the grain interactions. However, when the crystal plasticity method is employed in the finite element (FE) method, the stress equilibrium and strain compatibility are automatically achieved by the built-in ability of the FE solver for modelling polycrystals. With the introduction of the dislocation dynamics simulations by Devincre and Kubin [8, 9], the crystal plasticity method has been backed with a solid physical-based understanding from the elementary dislocation mechanism.

Since microcrack initiation smaller than the grain size highly depends on the grain arrangement, the prediction of microcrack initiation is normally based on the crystal plasticity framework. Fine and Bhat [10] proposed an energy approach to estimate the number of cycles to initiate microcracks in single crystal iron and copper, by balancing the energy required to form the crack surfaces and the energy released from storage. Voothaluru and Liu [11] applied the energy method into the crystal plasticity framework to predict crack initiation life for the randomly generated grain microstructures of a polycrystalline copper, and to identify the potential weak sites in fatigue behaviour. Tanaka and Mura [12] proposed a crack nucleation life rule based on the assumption that microcracks were initiated by irreversible dislocation pile-ups in PSB. Several works [13, 14] modelled the prediction of the crack initiation in polycrystalline steel based on Mura's rule, as well as investigated the relationship between crack densities, crack imitation rate and cycle number. In addition to the above method, there are a variety of crack initiation indicators developed to predict microcrack initiation sites and to determine the number of cycles leading to microcrack initiation, such as the accumulated plastic deformation $\mathrm{p} = \int_0^T \left(\frac{2}{3}\boldsymbol{L^p}:\boldsymbol{L^p}\right)^{\frac{1}{2}} dt$ in Manonukl and Dunne [15] and local plastic dissipation energy $\mathrm{E_p} = \int \boldsymbol{\sigma}:\boldsymbol{L_p}\, dt$ in Cheong et al. [16] . Therefore, it is important to understand the local stress and strain distribution based on a given grain orientation and grain arrangement. The crystal plasticity method, which predicts the macroscopic plastic behaviour by examining the microscopic anisotropic crystal behaviour, is a powerful tool to study the microstructure influence on the fatigue failure. The microscopic factors usually involve slip with the associated dislocation, texture and grain shape, in the context of continuum mechanics. However, it is also argued [17] whether these crack initiation indicators would lead to a fatal flaw. By comparing the crack initiation experimental

results by DIC and FE simulation results by crystal plasticity, Cheong et al [16] also pointed out that high energy sites are not necessarily the crack initiation sites; however, crack initiation sites must have high energy.

There are several studies which deal with austenitic steels including stainless steel 304L and 316L using CPFEM. Le Pécheur et al. [18] used the dislocation density-based model by constructing a 3D aggregate to investigate the effect of pre-hardening, which leads to a more homogeneous local stress and strain distribution at the stabilised fatigue region. In addition, a variety of damage initiation criteria were applied to aggregates of different surface roughness to investigate the sensitivity of these criteria to the roughness profile and pre-hardening. Feaugas and Pilvin [19] reviewed the dislocation pattern related to the hardening stages, and introduced the dislocation structure into the constitutive equations of a single crystal, including walls and channels. Li et al. [20, 21] considered the softening effect in the stainless steel and studied the overload effect and the influence of the loading path. Schwartz et al. [22] employed a non-local approach to account for the strain gradient between adjacent points, which gives a better prediction of the tensile and fatigue tests for materials of a variety of grain sizes. Guilhem et al. [23, 24] pointed out the cluster effect for the local fracture, such as grain location, grain arrangement and interaction. Sweeney et al. [25] compared the crack initiation sites observed from four-point bending test and those obtained from CPFEM simulation. Elastic anisotropy was found to be vital in the microstress and slip distributions. In addition, the locations of the peak density of geometry necessary dislocations were coincident with the peak effective plastic strain, dominant accumulated plastic slip and the experimentally observed crack initiation sites.

The aim of the current paper is to build up a framework of the CPFEM, and to investigate the crack initiation criterion based on this model. Section 2 introduces the theory of CPFEM, including the kinematics and hardening behaviour of a single crystal, as well as the transition rule between a single crystal and polycrystals. Section 3 outlines the experimental methodology relating to the model, including detailed procedure for material characterisation and the method for determining the material constants. Section 4 illustrates the CPFEM model development and the main simulation results. The experimental and modelling results are discussed and concluded in Section 5.

2 Theory

The crystal structure of the austenitic steel is FCC, which has only one set of slip system {111}<110>, and comprises a total of twelve slip systems that can take part in the plastic deformation. The stereographic projection of the FCC crystal and the list of all the available slip systems for FCC, as well as the notation of these slip systems corresponding to the stereographic projection can be referred to Zhang [26]. When the loading direction, presented in a standard triangle of the stereographic projection, falls into the inner part of a triangular domain, the indexed slip system inside the unit triangle would give the highest Schmid factor, which is called the primary slip system. However, when the loading direction falls onto the edges or vertices of the triangle, the slip systems adjacent to the edges or vertices are to be simultaneously activated [26]. Each slip system is under the same macroscopic loading and deformation gradient, and only the slip systems that have the highest Schmid factor are favoured for plastic deformation and would be activated first.

Two main stages are required in the crystal plasticity framework, the first is the transition model linking the microscopic and the macroscopic behaviour, and the second is constitutive equations of the single crystal plasticity. Detailed in-depth reviews of the crystal plasticity theory can be found in articles by Asaro [27, 28] and Roters et al. [29].

2.1 Single crystal constitutive equations

The model used in this paper was originally developed by Erieau and Rey [30]. The deformation gradient $\boldsymbol{F}$ can be decomposed into a lattice deformation gradient $\boldsymbol{F}^*$ and a plastic deformation gradient $\boldsymbol{F_p}$, by assuming that the material flows due to dislocation motion, and then the combination of elastic deformation and rigid body rotation [29]:

$$\boldsymbol{F} = \boldsymbol{F}^* \boldsymbol{F_p} \tag{1}$$

The velocity gradient $\boldsymbol{L}$ is defined as

$$\boldsymbol{L} = \dot{\boldsymbol{F}}\boldsymbol{F}^{-1} = \dot{\boldsymbol{F}}^*\boldsymbol{F}^{*-1} + \boldsymbol{F}^*\dot{\boldsymbol{F}}_{\boldsymbol{p}}\boldsymbol{F}_{\boldsymbol{p}}^{-\mathbf{1}}\boldsymbol{F}^{*-1} = \boldsymbol{L}^* + \boldsymbol{F}^*\boldsymbol{L_p}\boldsymbol{F}^{*-1} \tag{2}$$

The velocity gradient can be defined as the sum of a symmetric deformation tensor $\boldsymbol{D} = \frac{1}{2}[\boldsymbol{L} + \boldsymbol{L}^{\boldsymbol{T}}]$ and antisymmetric rotation velocity tensor $\boldsymbol{\Omega} = \frac{1}{2}[\boldsymbol{L} - \boldsymbol{L}^{\boldsymbol{T}}]$.

$$\boldsymbol{L} = \boldsymbol{D} + \boldsymbol{\Omega} \tag{3}$$

The deformation tensor and rotation tensor are both composed of a lattice contribution part and a plastic part, such that $\boldsymbol{D} = \boldsymbol{D}^{*} + \boldsymbol{D_p}$ and $\boldsymbol{\Omega} = \boldsymbol{\Omega}^{*} + \boldsymbol{\Omega_p}$.

The local crystal coordinate for the slip system α is defined by the slip direction $\boldsymbol{m}^{\alpha}$ and slip plane normal $\boldsymbol{n}^{\alpha}$ in the global coordinate. The plastic velocity tensor $\boldsymbol{L_p}$ is expressed by the sum of the shearing rate $\dot{\gamma}^{\alpha}$ for all the available 12 slip systems of a FCC crystal structure ($\alpha = 1,2, \ldots 12$), as follows:

$$\boldsymbol{L_p} = \sum_{\alpha=1}^{12} \dot{\gamma}^{\alpha}\, \boldsymbol{m}^{\alpha} \otimes \boldsymbol{n}^{\alpha} \tag{4}$$

$\otimes$ is the vector dyadic product. The crystal coordinate would remain the same if only the plastic deformation gradient is applied. However, the lattice deformation gradient $\boldsymbol{F}^{*}$ would transform the crystal coordinate into an intermediate coordinate, such that

$$\boldsymbol{m}^{*\alpha} = \boldsymbol{F}^{*} \cdot \boldsymbol{m}^{\alpha} \;\; and \;\; \boldsymbol{n}^{*\boldsymbol{\alpha}} = \boldsymbol{n}^{\alpha} \cdot \boldsymbol{F}^{*-1} \tag{5}$$

It is convenient, for the subsequent formulations, to introduce the concept of the Schmid factor $\boldsymbol{\mu^{\alpha}}$

$$\boldsymbol{\mu^{\alpha}} = \frac{\boldsymbol{1}}{\boldsymbol{2}}(\boldsymbol{m}^{*\alpha} \otimes \boldsymbol{n}^{*\boldsymbol{\alpha}} + \boldsymbol{n}^{*\alpha} \otimes \boldsymbol{m}^{*\boldsymbol{\alpha}}) \tag{6}$$

and lattice spin tensor $\boldsymbol{\omega^{\alpha}}$

$$\boldsymbol{\omega^{\alpha}} = \frac{\boldsymbol{1}}{\boldsymbol{2}}(\boldsymbol{m}^{*\alpha} \otimes \boldsymbol{n}^{*\boldsymbol{\alpha}} - \boldsymbol{n}^{*\alpha} \otimes \boldsymbol{m}^{*\boldsymbol{\alpha}}) \tag{7}$$

The shearing rate $\dot{\gamma}^{\alpha}$ for the slip system α was approximated by a power law, by assuming plastic flow occurs under all non-zero stresses without any yield condition or loading/unloading condition:

$$\dot{\gamma}^{\alpha} = \dot{\gamma}_0 \left(\frac{|\tau^{\alpha} - \chi^{\alpha}|}{g^{\alpha}}\right)^{n} sign(\tau^{\alpha} - \chi^{\alpha}) \tag{8}$$

where the resolved shear stress τ^{α} for the slip system α is the projection of the Kirchhoff stress tensor $\det(\boldsymbol{F})\,\boldsymbol{\sigma}$ onto the slip plane $\tau^{\alpha} = \det(\boldsymbol{F})\,\boldsymbol{\sigma}\colon \boldsymbol{\mu^{\alpha}}$, and it is the driving force of the plastic deformation. The backstress χ^{α}, which accounts for the Bauschinger effect [18], satisfies the nonlinear evolution rule:

$$\dot{\chi}^{\alpha} = C\dot{\gamma}^{\alpha} - D\chi^{\alpha}|\dot{\gamma}^{\alpha}| \tag{9}$$

The strength g^{α} for the slip system α represents the resistance of the plastic deformation, or the stress necessary to attain the reference velocity for the slip system α. The rate exponent *n(>1)* controls the strain rate sensitivity. As with the physical based hardening law, it is assumed that the dislocation cutting force is the major obstacle in plastic deformation, and the plastic shear rate is related to the mean effect of the mobile dislocation density [31]. The strength g^{α} is thus formulated with regards to the dislocation density ρ, such that:

$$g^{\alpha} = Gb\sqrt{\sum_{\beta=1}^{12} A_{\alpha\beta}\rho^{\beta}} \tag{10}$$

where $A_{\alpha\beta}$ are the entries of the 12×12 interaction matrix $\boldsymbol{A}$ in the α^{th} row and β^{th} column, describing the extent of hindering between different slip systems.

The entries of the interaction matrix $\boldsymbol{A}$ are indexed from a_0 to a_5, representing six dislocation interaction types proposed by Bassani and Wu [32], where a_0 represents self-interaction, a_1 represents collinear interaction, $a_2$represents formation of Hirth locks, a_3 represents interaction with coplanar dislocation, a_4 represents formation of

glissile junction, and a_5 represents formation of Lomer-Cottrell locks or sessile junctions.

The dislocation density evolution law [18] is able to describe the dislocation multiplication and annihilation for the slip system α, as follows:

$$\dot{\rho}^{\alpha} = \frac{|\dot{\gamma}^{\alpha}|}{b}\left[\frac{1}{D_{grain}} + \frac{\sqrt{\sum_{\alpha\neq\beta}\rho^{\beta}}}{K} - 2y_c\rho^{\alpha}\right] \quad (11)$$

where b is the amount of Burgers vector. The term $1/D_{grain}$ introduces the grain effect so that with larger grain size, the dislocation density evolutions would be slower. The term $\sqrt{\left(\sum_{\alpha\neq\beta}\rho^{\beta}\right)}/K$ controls the dislocation formation, and the constant y_c represents the critical annihilation length, which is related to dynamic recovery.

In order to formulate the constitutive equations for the material, the co-rotational stress rate on axes rotating with the material results from both the material deformation and rigid body rotation, as follows

$$\overset{\nabla}{\boldsymbol{\sigma}} = \boldsymbol{\mathcal{L}}:\boldsymbol{D}^{*} - \boldsymbol{\sigma}(\boldsymbol{I}:\boldsymbol{D}^{*}) - \boldsymbol{\Omega_p}\boldsymbol{\sigma} + \boldsymbol{\sigma}\boldsymbol{\Omega_p} \quad (12)$$

where $\boldsymbol{\mathcal{L}}$ is the 4th order elastic stiffness tensor.

2.2 Polycrystal morphology and homogenization method

There have been a variety of transition models proposed historically to transit the output from the micro-scale to the macro-scale, including the fully constrained model by assuming a uniform plastic strain [7], a uniform stress or a uniform total strain, which has been reviewed by Van Houtte [33]. Self-consistent methods [34] consider the grain interaction. The deformation field approximations all assumed homogeneous stress and strain inside an individual grain, but they differed in the treatment of grain interaction. However, Roters [29] pointed out that it was important to choose the appropriate transition model for a certain loading situation.

With the development of FE solvers, the crystal plasticity framework was incorporated into the FE software codes. CPFEM has the advantage in the transition treatment from micro-scale to macro-scale, since CPFEM considers the grain interactions, so that it satisfies both the stress equilibrium and strain compatibility. Becker [35] was the first to simulate the FCC crystal of 12 slip systems in the framework of crystal plasticity in the ABAQUS FE software. The CPFEM also has the ability to solve complex loading systems with complex geometries and anisotropic texture.

CPFEM uses the continuum mechanics theory incorporating a statistical model in the simulating process. A number of grains are constructed as a representative volume element (RVE), to represent the bulk polycrystalline aggregates. The roles of the aggregate construction, element type and size were investigated in [36, 37]. The minimum size of the RVE depends on the loading conditions and the material texture, though it is generally agreed that 10^3 to 10^4 numbers of grains are recommended to ensure that the grain number is large enough to represent the macroscopic behaviour of a material containing the order of billions of grains statistically.

In this study, the mean-field homogenization method was used, in which the macroscopic quantities equal the volume-weighed sum of those over microstructural domains [29]. The macroscale stress $\bar{\boldsymbol{\sigma}}$ and strain $\bar{\boldsymbol{\varepsilon}}$ are the volume-averaged values computed from the local stress and strain of the whole domain $\mathcal{B}$ as follows:

$$\bar{\boldsymbol{\sigma}} = \frac{1}{V}\int_{\mathcal{B}}\boldsymbol{\sigma}\,dV \quad (13)$$

and

$$\bar{\boldsymbol{\varepsilon}} = \frac{1}{V}\int_{\mathcal{B}}\boldsymbol{\varepsilon}\,dV \quad (14)$$

3 Material Characterization

A bar made of commercial 304 stainless steels was used to conduct a series of experiments to examine the material composition, microstructure, and nanostructure. Strain controlled fatigue tests were conducted to obtain the bulk mechanical behaviours. Information obtained from these experiments, such as average grain size, lattice parameter, dislocation density and fatigue loops, was later to be used in FE simulation for determining part of the material constants and creating the model geometry. In addition, the fractured surfaces were also examined under SEM to investigate the fracture mode.

3.1 Material Composition

The material composition of the bulk material was examined via spark-optical emission spectrometry (OES) (Table 2), called Foundry master. This is a fast and precise technology for pure metals. The results obtained show that the material compositions are within the scatter band of the requirement for a standard material composition of 304 stainless steel [38], except that the concentration in element S 0.17% is higher than the recommended value of less than 0.03% in weight.

Table 2. Material Composition (% in weight) obtained by Foundry master

Fe	C	Si	Mn	P	S	Cu	Cr
69.7	0.062	0.366	1.98	0.023	0.17	0.671	17
Mo	Ni	Al	Co	Nb	Ti	V	W
0.41	9.37	0.002	0.108	0.034	0.005	0.061	0.035

3.2 Uniaxial tensile test

The complete stress-strain curve of tensile specimens obtained from the uniaxial tensile test is shown in Fig. 1. Young's modulus is calculated to be 190GPa, and the 0.2% offset yield stress is 520MPa. The material exhibits some extent of cold working before the tensile test, which may result from the manufacturing of the raw material, as well as manufacturing of the tensile specimens. The ultimate tensile strength is 759MPa and elongation at fracture is 47%, which show higher than normal yield strength, which is assumed to be caused by pre-hardening.

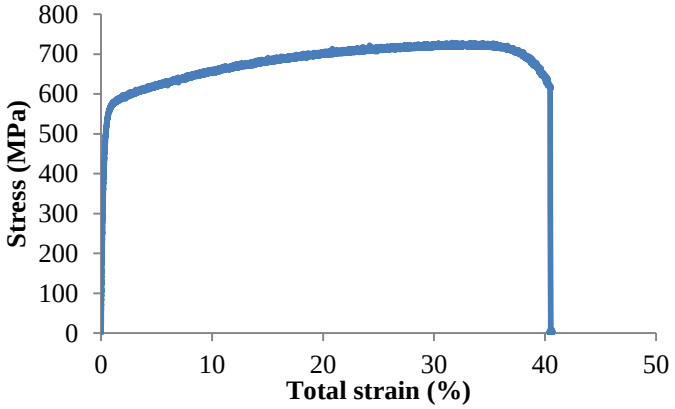

Fig. 1 Stress-strain curve in the tensile tests

3.3 Uniaxial fatigue tests

Fatigue specimens of cylindrical cross-section were manufactured from the as-received material, based on the geometry and length requirement specified by the relevant British standard [39], as shown in Fig. 2 In order to ensure the central alignment of the specimen to the load actuator, the specimen ends were designed as cylindrical grips. The

dimensions of the specimen were set to have gauge diameter *d=7mm*, parallel length *l=14mm*, radius r=30mm, grip diameter *D=14mm*, and grip length *50mm*.

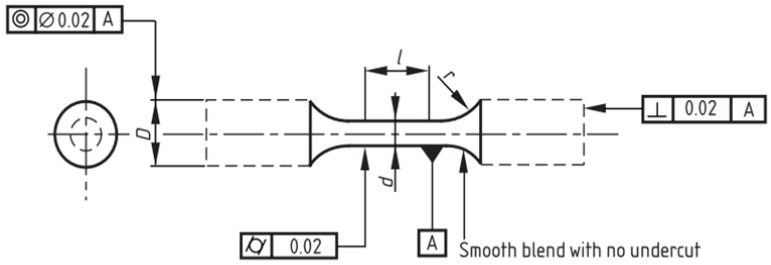

Fig. 2 Geometry for the cylindrical fatigue specimen, dimensions in millimetres [39]

A series of strain controlled fatigue tests at room temperature and at a frequency of 0.1Hz were conducted on an Instron Servohydraulic test machine 8801. The fatigue tests stop when the maximum cyclic load drops by 99% compared with the reference cycle number 10 to ensure that the specimen fractures into two pieces at the end of fatigue tests. The stress amplitude evolutions against cycle number in the logarithmic scale for specimens at the strain ranges of $\pm 0.4\%$, $\pm 0.5\%$ and $\pm 0.6\%$ are plotted at Fig. 3.

It was noted that under cyclic loading within the initial 10 cycles, there was always a rapid hardening. After initial fast cyclic hardening, the material exhibited cyclic softening to a stabilized region before failure. The stabilised region is proposed to be resulted from the development of the unique dislocation structure corresponding to a unique applied loading [40]. The relationship between the dislocation structure and the applied loading can be referred to the work by Mughrabi [41] and the review by Feaugas and Pilvin [19].

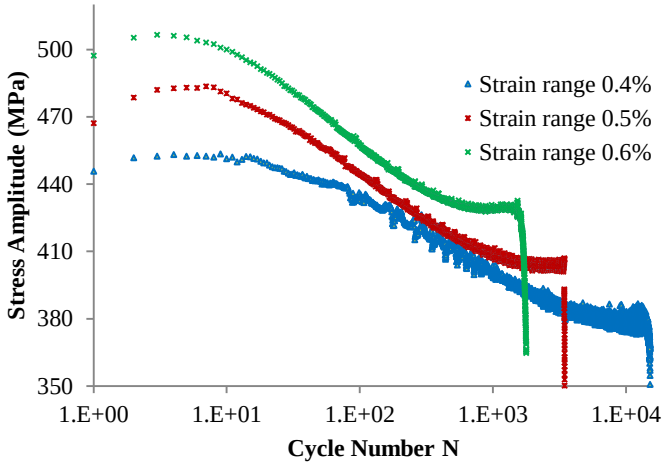

Fig. 3 Stress amplitude against cycle number of the strain controlled fatigue tests at room temperature

For example, fatigue test at strain range of $\pm 0.6\%$ stopped at cycle number 1790, and a dominant crack of length 5mm was observed. Before fracture, there is a stabilised region between cycle number 500 and 1700. In order to further understand the cyclic stress-strain behaviour during the fatigue test, the hysteresis loops at cycle numbers 10, 800 and 1780 are plotted in Fig. 4. The amount of the plastic deformation of each cycle can be represented by the length of the two intersection points of the hysteresis loop and the x-axis. After the initial softening, more plastic deformation was observed. In addition, there is no obvious degradation of the effective Young's modulus until near fracture when N=1780.

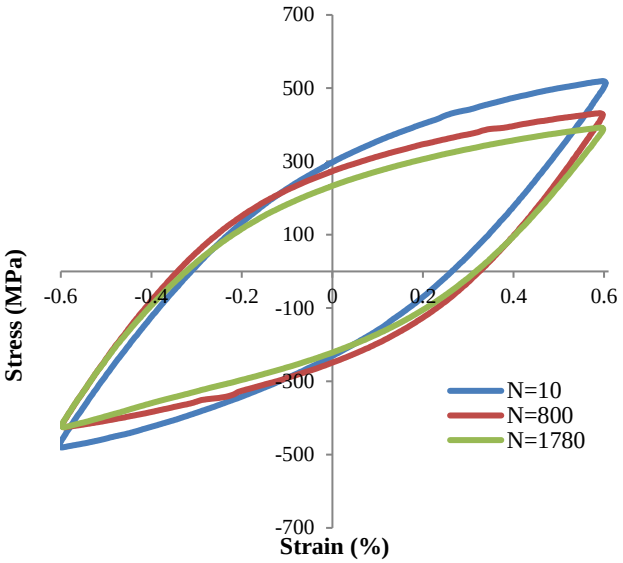

Fig. 4 Hysteresis loops for the fatigue test at strain range of ±0.6%, and cycle numbers of N=10, N=800 and N=1780

3.4 Microstructure

The Philips/FEI XL-30 scanning electron microscope (SEM) was used in this work with an accelerating voltage of 20kV and a working distance of 10mm. The sample was hot mounted in electrically conductive phenolic resin in order to facilitate grinding and polishing. Samples were flattened using a coarse grade of silicon carbide paper and then progressively ground by finer grades until a surface roughness of 1μm was achieved.

The SEM image under the secondary electron detector of the as-received material without etching is shown in Fig. 5(a). There were small dark dots all over the sample surface without being surrounded by bright rings, if observed under the secondary electron detector. However, if observed under the backscatter detector, they appeared as dark dots surrounded by bright rings, which is an indication that these dots are precipitates.

These precipitates and the surrounding matrix were further examined under energy dispersive spectroscopy (EDS), and the result indicates that the precipitates are composed of 25% sulphate, 10% chromium, 40% manganese and 22% iron by weight. Therefore, these inclusions may be a mixture of MnS, FeS and CrS.

The samples were then electro-etched by 65% nitric acid under direct current between 6 to 8 volts for 25-30 seconds, to reveal grain boundaries, and the SEM image is shown in Fig 5(b). The average grain size can be approximated by the line interception method, by drawing five random lines and counting the number of grains the lines come across. The average grain size is calculated by dividing the total length of the random lines by the number of grains. Based on the SEM results in Fig. 6 for the as-received material, the average grain size is 19 μm.

(a)

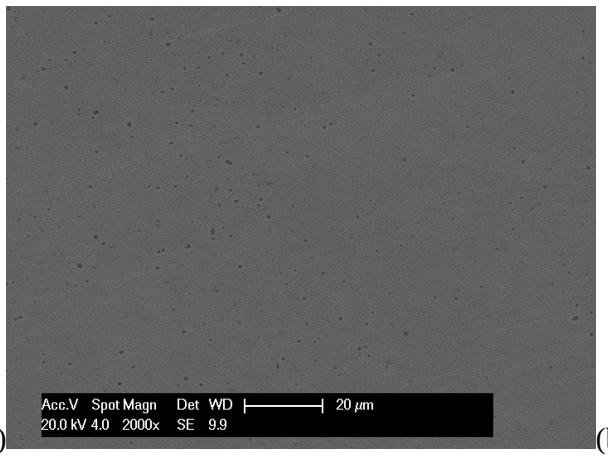

(b)

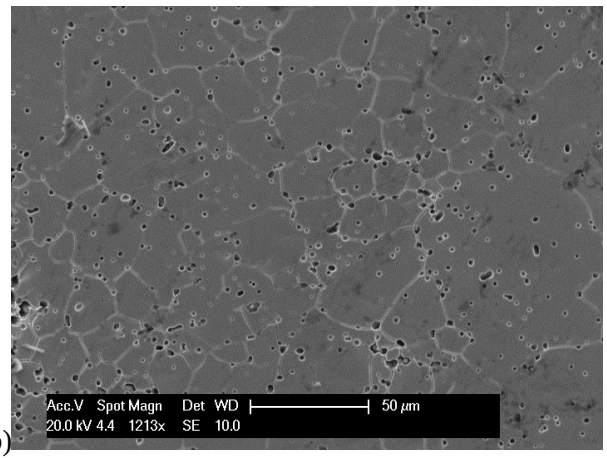

Fig. 5 SEM images for the as-received sample under the secondary electron detector (a) without etching; (b) after etching

3.5 Nanostructure

JEOL 2000FX Transmission electron microscopy (TEM) is used to obtain information on the nanoscale at higher magnifications, such as dislocation densities at the as-received condition, which is relavant in CPFEM. The sample was prepared by cutting thin slices of thickness 0.5*mm*. These slices were mounted onto a brass holder, and ground on a rotating coarse silicon carbide paper P240 to a thickness about 500 μm. Afterwards, these thin samples were punched using a mechanical puncher into a 3*mm* diameter disc, and then further ground to less than 200 μm manually and tenderly by silicon carbide paper P240, P400, P800 and P1200 separately, in order to achieve a flat and smooth surface for the two sides of the sample. Finally, the 3*mm* diameter disc sample was perforated in a thin foil preparation unit by electro-polishing, emerged in the electrolyte with a rim support. The chemical solution of the electrolyte is made up of 161*ml* ethanol, 46*ml* glycerol (which makes the solution viscous and flowing slowly), and 23*ml* $HClO_4$ at 0°C and 12V[42] . At low temperature, it was observed that there was nearly no current variation, by changing the voltage between 10V to 20V [43].

Mass-thickness contrast, diffraction contrast and phase contrast are three major contrast mechanisms to understand the TEM results. Among them, diffraction contrast is most likely to be responsible for the image formation of a thin foil for this material. In theory, when the beam strikes the lattice plane in the Bragg angle, the majority of the electrons would be diffracted. In contrast, when the beam is slightly tilted, then the majority of the electrons would pass through the aperture directly without diffraction.

Fig. 6 shows the TEM images for the as-received specimen, Fig. 6(a) shows the matrix microstructure of about 300 *nm* in size, compromising vein-like dense arrays of edge dislocations. Fig. 6(b) shows dark bands representing the strain field, and several straight and parallel lines presenting defects, which can be twins, stacking faults and grain boundaries. Fig. 6(c) contains the dark regions on the left side but bright regions on the right, because the thin sample has buckled. The bright region is at an orientation, which slightly deviates from the Bragg condition so that most electrons go through the lattice without being diffracted. However, the sample tilt resulted from sample preparation and the existence of dislocations diffracts part of the electron, so that the left side appears to be slightly darker. In addition, dislocations are also visible. The dislocation density can be roughly calculated by the line intercept method [44], by drawing five random lines through the TEM images with total length L_r and counting the number of the intersection points *N*, with the following equation:

$$\rho = N/L_r t \tag{15}$$

in which *t* is the thickness of the TEM foil, normally about 50nm. The order of magnitude of the dislocation densities is 1×10^8 mm^{-2}. One limitation of the method to calculate the dislocation density is that the observation area of the TEM sample is extremely small, which is unable to provide a general outlook of the average dislocation density over the loading area.

The TEM images up to now were obtained by a single tilt support only. However, a double tilt support would be used in the further analysis of the microstructure evolution of the fractured specimens. In addition, the metallurgical preparing method used results in small thin regions and little information about defects near the hole, and more attempts would be needed to obtain TEM samples with better quality by slowing down the electro-polishing speed.

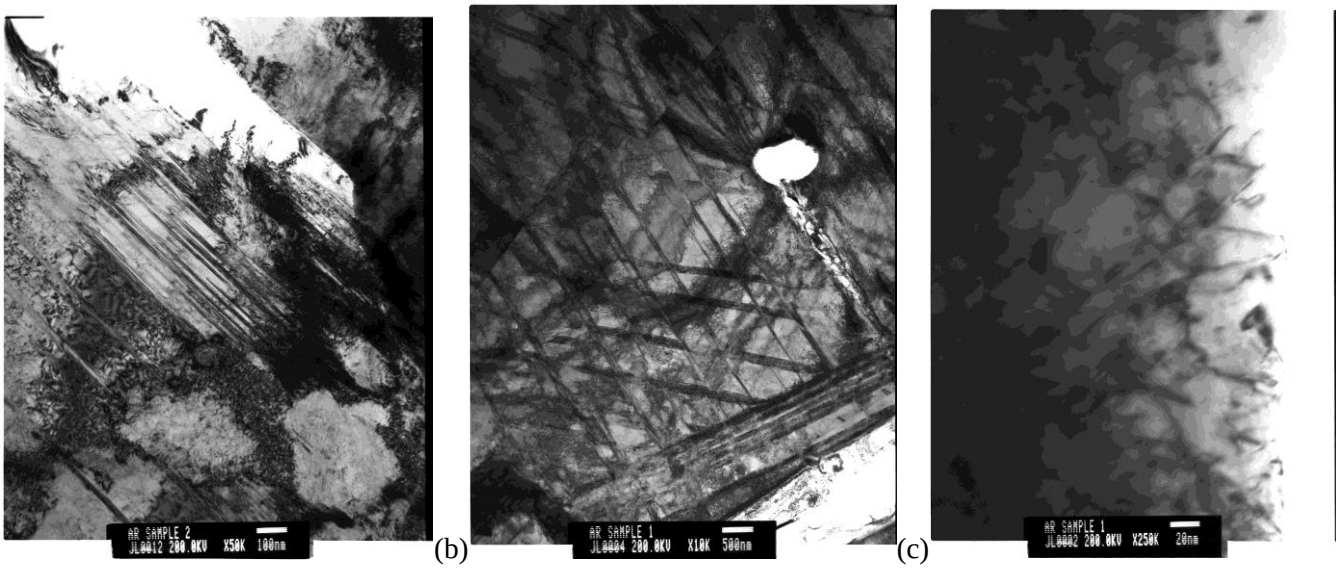

(a) (b) (c)

Fig. 6 TEM result: (a) Matrix microstructure containing vein-like dislocations; (b) Stacking faults and matrix microstructure; (c) Dislocations

3.6 Crystal structure

The crystal structure of the material can be examined by X-ray diffractometer (XRD). The diffraction spectrum is recorded by rotating the X-ray detector at the rate of $2\dot{\theta}$ about the sample, which is mounted on the goniometer stage rotating at the rate of $\dot{\theta}$. The diffraction spectrum (Fig. 7) shows the diffraction angles 2θ for the reflection planes (111), (200), (220), (311), (222) and (400), which is governed by Bragg's law

$$n\lambda = 2dsin\theta \tag{16}$$

where n is an integer representing the order of reflection, and λ represents the wavelength of the CuK_α radiation ($\lambda = 0.1540598nm$) here. The parameter d_{hkl} is the spacing of lattice planes (hkl), which is related to the lattice parameter a as follows:

$$a = d_{hkl}/\sqrt{h^2 + k^2 + l^2} \tag{17}$$

The diffraction spectrum was analysed by comparing the diffraction angles and their intensities to the standard powder diffraction spectrum from the Joint Committee of Powder Diffraction Standards, which is built into the analysing software of the XRD data. It was found that there are two phases existing, austenite and pure iron. The diffraction angles 2θ of both phases were reasonably larger than the angles defined in the database, since both phases have some extent of pre-hardening.

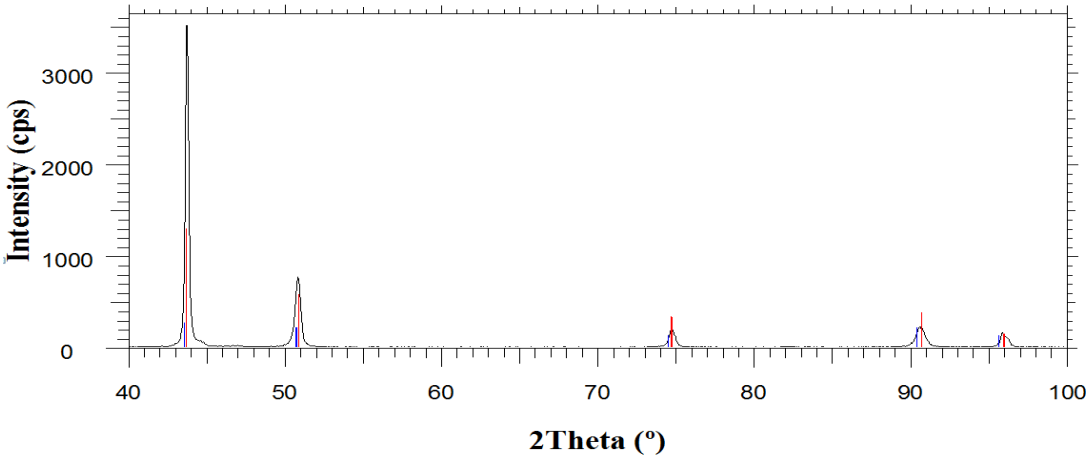

Fig. 7 Diffraction spectrum by plotting scattering angle 2θ against the relative intensity, showing red austenitic peaks and blue iron peaks from powder database spectrum.

The lattice parameter a of the austenitic phase can also be determined from individual planar spacing d_{hkl}, as shown in Table 3. These obtained lattice parameters were plotted against the function $\cos(2\theta)/\sin(\theta)$, and the beast value with least error is obtained by extrapolating the data to $2\theta = \pi$ [45]. This method is plotted in Fig. 8, and the lattice parameter at $\cos(2\theta)/\sin(\theta) = -1$ is calculated to be $a = 0.3584nm$. The amount of Burgers vector of a perfect dislocation is calculated to be

$$b = \frac{a}{2}\langle 110\rangle = 0.2534nm \tag{18}$$

In addition, there are intensity anomalies, because the grains are not randomly oriented in space, resulting from the texture obtained from the manufacturing process, such as drawing.

Table 3 A list of Bragg's angle, their corresponding reflection plane and the obtained lattice parameter

Bragg's Angle 2θ (°)	Planar Spacing d (nm)	Reflection Plane (hkl)	Lattice Parameter a (nm)
43.8	0.2065	(111)	0.3577
51.0	0.1789	(200)	0.3578
74.8	0.1268	(220)	0.3587
90.8	0.1082	(311)	0.3588
96.0	0.1037	(222)	0.3590

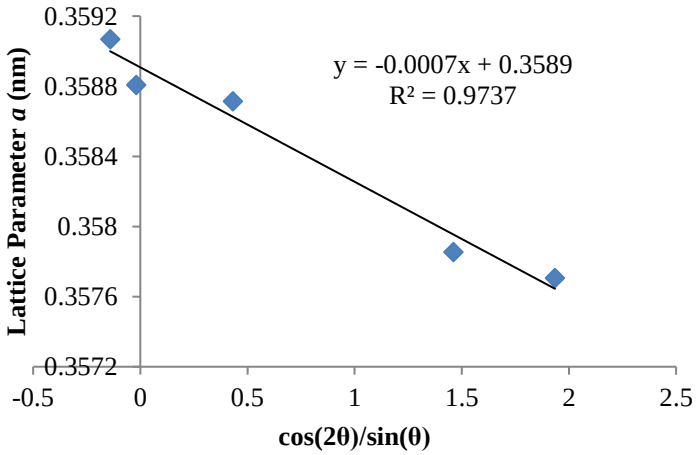

Fig. 8 The lattice parameter determination method by extrapolating the data to $2\theta = \pi$.

Bruker D8 Discover X-ray diffractometer is a kind of advanced XRD capable of diffraction measurements from relatively small areas. The machine maps the density distribution diffracted by a particular family of crystal planes with regard to the sample frame, and allows measurements of crystallographic texture. The scanning was only conducted from 0° to 70° relative from the surface. After background processing, the results were plotted as the pole figures of plane groups of {111}, {200} and {220} inclined to the bar axis at an angle from 0° to 70° (Fig. 9). The diffraction density is proportional to the intensity of black colour.

The material is lightly textured such that the plane group of {111} lies parallel to the specimen bar axis, as observed from the pole Fig. of the plane group of {111}. The pole Fig. of the plane groups of {200} and {220} shows a high density of poles in a circular shape of radius r inside the pole Fig. of radius R at an inclination angle of 90°. The concentric circles in the pole Fig.s indicate that the corresponding planes share the same angle of α to the central bar axis, satisfying

$$r/R = \tan(\alpha/2) \quad (19)$$

For example, the plane (111) has an angle of 54.7° with the plane (200), and an angle of 35.3° with the plane (220). Therefore, the plane (111) contributes to the high density in a circular shape with radius ratio $r/R = 0.52$ in pole Fig. of plane group of {200} and $r/R = 0.32$ in the pole figure of the plane group of {220}. Based on the same principle, the plane (200) contributes to $r/R = 0.52$ in the pole figure of plane group of {111} and $r/R = 0.41$ in pole Fig. of plane group of {220}.

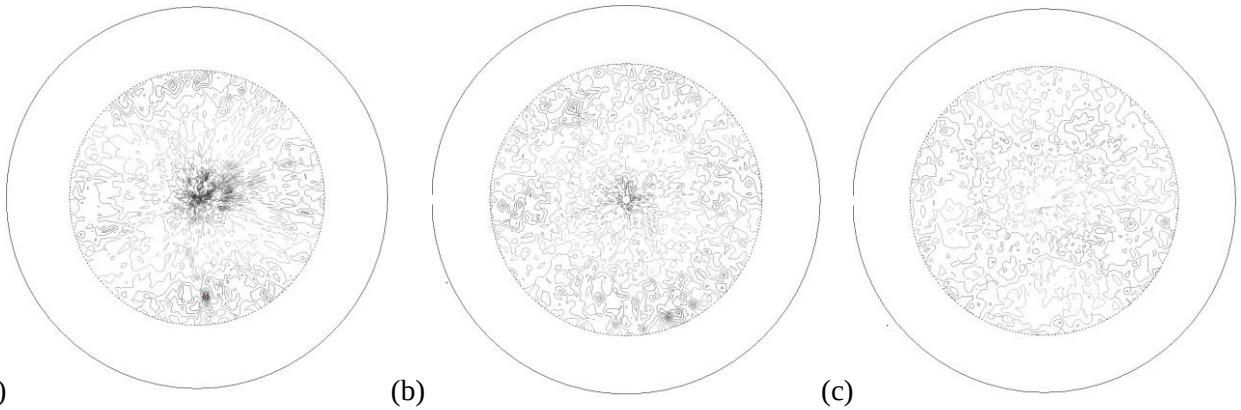

(a) (b) (c)

Fig. 9 Pole figures of poles: (a) {111}; (b) {200}; (c){220}.

3.7 Fractured surface

The specimens progressively continued to fracture during the fatigue tests. There are two kinds of failure modes observed on the fractured surface. Half of the fractured surface broken initially by fatigue is bright and level, while the other half is dark and rough with some necking effects caused by ductile fracture afterwards, if observed by the naked eye. Fig. 10(a) shows the fractured surface for the fatigue test at the strain range of 0.5% under SEM by both fatigue and ductile fracture.

By zooming into the fatigue fractured surface (Fig. 10(b)), there are small cracks which are prone to develop at grain boundaries, revealing the grain size. Fatigue striations form inside the grains near the grain boundary. In addition, evident inclusions in pores are observed. The ductile fracture surface (Fig. 10(c)) shows dimples of various sizes. In addition, inclusions are observed in most dimples.

The chemical composition of these inclusions were examined under EDS, and were composed of 25% sulphate, 11% chromium, 37% manganese and 27% iron by weight, which is similar to the weight composition of the precipitate in the as-received material. Therefore, these inclusions may be a mixture of MnS, FeS and CrS. Under the influence of the applied load, the inclusions are assumed to be precursor sites for micro-crack initiation at the fatigue fracture surface, and produce pores near the inclusions at the ductile failure stage.

(a)

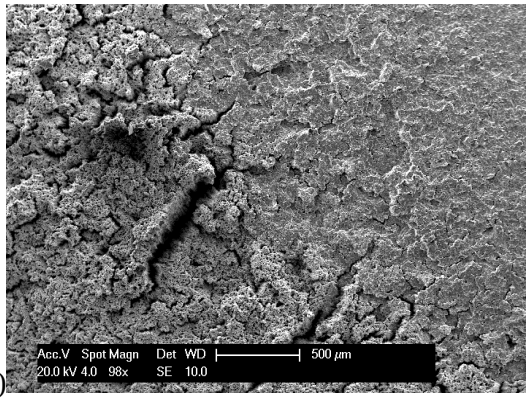

(b)

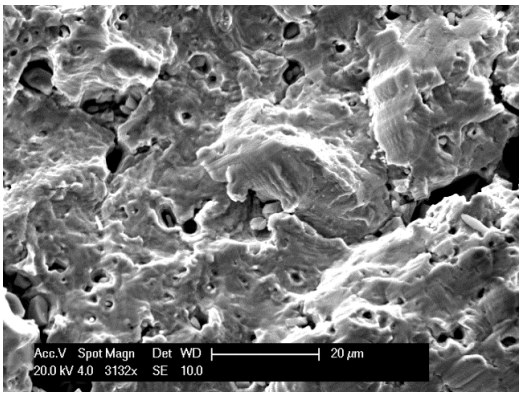

(c)

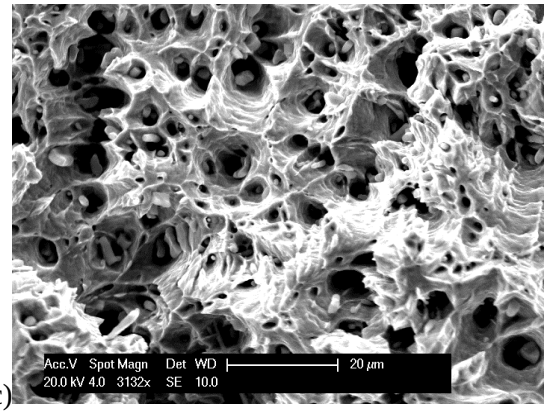

Fig. 10 (a) SEM image of the fractured surface showing the two different types of fracture occurred in fatigue test for 0.5%; (b) Upper right part bright and smooth, fatigue striations, evident inclusion and holes; (c) lower left part dark, dimpled surface.

4 **Finite Element Analysis**

The commercially available software ABAQUS implicit solver was used to implement CPFEM, which is able to analyse the stress, strain and energy distribution for a given geometry, material behaviour model, loading condition, and FE mesh specification. The Newton-Raphson method is employed in the implicit solver to solve the nonlinearities. When a particular nonlinear material constitutive behaviour is not available in the ABAQUS material libraries, a UMAT subroutine is an alternative for the user to code the material behaviour, written in the FORTRAN language. The numerical process of updating the stress and Jacobian matrix required by the UMAT subroutine is described in detail in section 4.1, while the development of the FE model and FE results are presented in sections 4.2. and 4.3. The complete UMAT code was developed by the present authors.

4.1 UMAT subroutine

The first step in coding the UMAT subroutine for the constitutive equations for a single crystal is to transform the local crystal coordinate to the global coordinate based on the grain orientation. The details of the coordinate transformation are given in Appendix A.

The second step is to establish a numerical integration scheme to update the stress from the nonlinear set of constitutive equations for a single crystal. There are a lot of different numerical schemes for integrating the constitutive equations of the elasto-viscoplastic behaviour of a single crystal [46-48]. One of the numerical methods proposed by Asaro and Needleman [49] and Huang [50] for small deformations is used here. In this method, a Newton-Raphson method is used to numerically calculate the shear strain increment for all the 12 available slip systems by minimising the residual function R^{α}, as follows:

$$R^{\alpha} = \frac{\Delta\gamma^{\alpha}}{\Delta t} - (1-\theta)\dot{\gamma}_t^{\alpha} - \theta\dot{\gamma}_{t+\Delta t}^{\alpha} \tag{20}$$

where the parameter θ, ranging from 0 to 1, is a user-defined parameter used to indicate the time integration scheme used. $\theta = 0$ corresponds to the forward Euler time integration scheme, which can experience problems of numerical stability. In order to ensure stability and convergence, a value between 0.5 and 1 is often chosen [51]. $\dot{\gamma}_t$ represents the shear strain rate in the current time point, and $\dot{\gamma}_{t+\Delta t}$ represents the shear strain rate in the next time point.

The initial guesses for the incremental slip strains $\Delta\gamma^{\alpha}$ of the Newton Raphson method are obtained by solving $R^{\alpha} = 0$, based on Taylor expansion of $\dot{\gamma}_{t+\Delta t}$, as follows:

$$\dot{\gamma}_{t+\Delta t}^{\alpha} = \dot{\gamma}_t^{\alpha} + \frac{\partial\dot{\gamma}^{\alpha}}{\partial\tau^{\alpha}}\Delta\tau^{\alpha} + \frac{\partial\dot{\gamma}^{\alpha}}{\partial g^{\alpha}}\Delta g^{\alpha} + \frac{\partial\dot{\gamma}^{\alpha}}{\partial\chi^{\alpha}}\Delta\chi^{\alpha} \tag{21}$$

In order to solve for incremental slip strains, $\Delta\tau^{\alpha}$, Δg^{α} and $\Delta\chi^{\alpha}$ are expressed as functions of $\Delta\gamma^{\beta}$ separately. The incremental form of Schmid stress is expressed as

$$\Delta\tau^{\alpha} = \lambda_{ij}^{\alpha}(\Delta\varepsilon_{ij} - \textstyle\sum_{\beta}\mu_{\mathrm{ij}}^{\beta}\,\Delta\gamma^{\beta}) \tag{22}$$

where $\lambda_{ij}^{\alpha} = L_{ijkl}\mu_{\mathrm{kl}}^{\alpha} + \omega_{ik}^{\alpha}\sigma_{jk} + \omega_{jk}^{\alpha}\sigma_{ik}$ based on the rotated slip system coordinate. The incremental form of strength for each slip system is

$$\Delta g^{\alpha} = \textstyle\sum_{\beta} h_{\alpha\beta}\left|\Delta\gamma^{\beta}\right| \tag{23}$$

Based on the dislocation density evolution law, the hardening matrix $h_{\alpha\beta}$ is expressed by

$$h_{\alpha\beta} = \frac{GA^{\alpha\beta}}{2\sqrt{\sum_{\beta=1}A^{\alpha\beta}\rho_F^{\beta}}}\left[\frac{1}{D_{grain}} + \frac{\sqrt{\sum_{\beta=1}a^{\alpha\beta}\rho_F^{\beta}}}{K} - 2y_c\rho^{\alpha}\right] \tag{24}$$

The incremental form of the back stress is

$$\Delta\chi^{\alpha} = C\Delta\gamma^{\alpha} - D\chi^{\alpha}|\Delta\gamma^{\alpha}| \tag{25}$$

The initial guesses for the incremental slip strains are given by solving a set of linear equation $R^{\alpha} = 0$ based on Taylor expansion, as follows:

$$\sum_{\beta}\left\{\delta_{\alpha\beta} + \theta\Delta t\frac{\partial\dot{\gamma}^{\alpha}}{\partial\tau^{\alpha}}\lambda_{ij}^{\alpha}\mu_{\mathrm{ij}}^{\beta} - \theta\Delta t\frac{\partial\dot{\gamma}^{\alpha}}{\partial g^{\alpha}}h_{\alpha\beta}sign(\Delta\gamma^{\beta}) - \theta\Delta t\frac{\partial\dot{\gamma}^{\alpha}}{\partial\chi^{\alpha}}\left[C - D\chi^{\alpha}\mathrm{sign}(\Delta\gamma^{\beta})\right]\delta_{\alpha\beta}\right\}\Delta\gamma^{\beta}$$

$$= \dot{\gamma}_t^{\alpha}\,\Delta t + \theta\Delta t\frac{\partial\dot{\gamma}^{\alpha}}{\partial\tau^{\alpha}}\lambda_{ij}^{\alpha}\Delta\varepsilon_{ij} \tag{26}$$

The modified incremental slip strain $\delta\Delta\gamma^{\alpha}$ is calculated using the Newton-Raphson iteration

$$R^{\alpha}+\frac{\partial R^{\alpha}}{\partial \Delta\gamma^{\beta}}\delta\Delta\gamma^{\beta}=0\rightarrow\sum_{\beta}\begin{Bmatrix}\delta_{\alpha\beta}+\theta\Delta t\frac{\partial\dot{\gamma}^{\alpha}}{\partial\tau^{\alpha}}\lambda_{ij}^{\alpha}\mu_{ij}^{\beta}-\theta\Delta t\frac{\partial\dot{\gamma}^{\alpha}}{\partial g^{\alpha}}h_{\alpha\beta}sign\left(\Delta\gamma^{\beta}\right)\\-\theta\Delta t\frac{\partial\dot{\gamma}^{\alpha}}{\partial\chi^{\alpha}}\left[C-D\chi^{\alpha}\text{sign}(\Delta\gamma^{\beta})\right]\delta_{\alpha\beta}\end{Bmatrix}\delta\Delta\gamma^{\beta}=-R^{\alpha}\quad(27)$$

The previous incremental slip strains $\Delta\gamma^{\alpha}$ is updated to $\Delta\gamma^{\alpha}+\delta\Delta\gamma^{\alpha}$, until the absolute residual is within a specific tolerance $|R^{\alpha}|<\delta_{tol}$, or the iteration number reaches the maximum allowed number of iterations N_{iter}.

In the UMAT subroutine coding with orientation-related material behaviours, the stress component is in the local system. The co-rotational stress increment is updated as follows:

$$\Delta\sigma_{ij}=L_{ijkl}\Delta\varepsilon_{kl}-\sigma_{ij}\Delta\varepsilon_{kk}-\sum_{\alpha=1}^{12}\lambda_{ij}^{\alpha}\Delta\gamma^{\alpha}\quad(28)$$

The final step in coding the UMAT subroutine is to update the Jacobian matrix, which is defined as the change of stress increment with respect to strain increment, as follows:

$$\frac{\partial\Delta\sigma_{ij}}{\partial\Delta\varepsilon_{kl}}=L_{ijkl}-\sigma_{ij}\delta_{kl}-\sum_{\alpha=1}^{12}\lambda_{ij}^{\alpha}\frac{\partial\Delta\gamma^{\alpha}}{\partial\Delta\varepsilon_{kl}}=L_{ijkl}-\sigma_{ij}\delta_{kl}-$$

$$\sum_{\alpha=1}^{12}\frac{\lambda_{ij}^{\alpha}\cdot\left(\theta\Delta t\frac{\partial\dot{\gamma}^{\alpha}}{\partial\tau^{\alpha}}\lambda_{kl}^{\alpha}\right)}{\left\{1+\theta\Delta t\frac{\partial\dot{\gamma}^{\alpha}}{\partial\tau^{\alpha}}\lambda_{ij}^{\alpha}\mu_{ij}^{\alpha}-\theta\Delta t\frac{\partial\dot{\gamma}^{\alpha}}{\partial g^{\alpha}}h_{\alpha\alpha}sign(\Delta\gamma^{\alpha})-\theta\Delta t\frac{\partial\dot{\gamma}^{\alpha}}{\partial\chi^{\alpha}}[C-D\chi^{\alpha}\text{sign}(\Delta\gamma^{\alpha})]\right\}}\quad(29)$$

When the UMAT was implemented in the current work, the numerical constants were set as $\theta=0.5$, and the maximum iteration number $N_{iter}=40$. $\frac{\Delta\gamma^{\alpha}}{\Delta t}$ is normally of the order of 10^{-4} to 10^{-3}, and the convergence tolerance δ_{tol} for $\frac{\Delta\gamma^{\alpha}}{\Delta t}$ is set to 1×10^{-5}.

4.2 FE model and material constants determination

In order to investigate the grain orientation and grain interaction effect on local stress-strain behaviour in the fatigue test, an illustrative model of a 3D cuboid shape is constructed with 25 grains as shown in Fig. 11 with dimensions of $76\mu m\times76\mu m\times19\mu m$. The random grain shape was constructed by the Voronoi tessellation method [37], which is rooted in physical processes such as solidification or recrystallization, when the grains are nucleated at a set of seed points generated randomly with a mean distance of $19\mu m$, and grow isotropically at the same rate [52] by the algorithm available in the MATLAB software. Each grain in the FE geometry was assigned with an orientation, and the distribution of the loading direction (010 in the global coordinates of ABAQUS) was presented in the inverse pole figure with vertices $[001]$, $[0\bar{1}1]$ and $[1\bar{1}1]$, as shown in Fig. 12 enclosing the slip system C3 $(11\bar{1})[101]$. Considering the boundary effect, the stress and strain distributions of grains located at the edges are not considered. For the rest of the grains in the FE geometry, their grain orientations were assigned purposely with hard grains No. 8, 12, 14 and 18 located near three vertices, and soft grains No. 7, 9, 13, 17 and 19 located in the central standard triangle. Although the grain orientation arrangement does not reflect the real textured material, it provides a good comparison between grains of different grain orientations.

The element type used is a 3D four-node tetrahedral element (C3D4 in ABAQUS), so that the grain boundaries are coincident with the element boundaries. In FE analysis, the nodal stress values are obtained via extrapolation and interpolation from the integration points of the elements, and thus these values may not be very accurate at the grain boundary, particularly if a relatively large element is used. In order to allow for the intragranular deformation, each grain is divided into a number of linear elements. The model is subjected to a strain-controlled loading within the range of $\pm0.2\%$ in the y-direction on Face 1. Face 2 is fixed in the x, y and z directions to prevent rigid body motion.

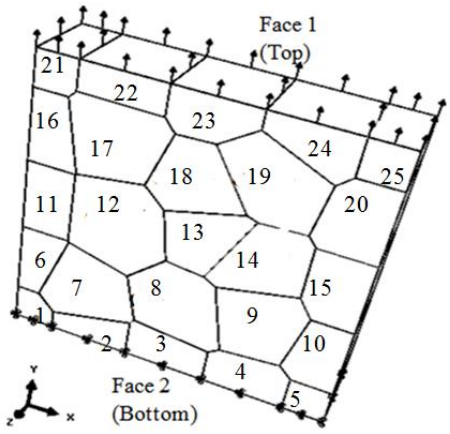

Fig. 11 A sketch of the polycrystal FE model. Face 1: strain controlled y-directional loading; Face 2: fixed in the x, y, z directions;

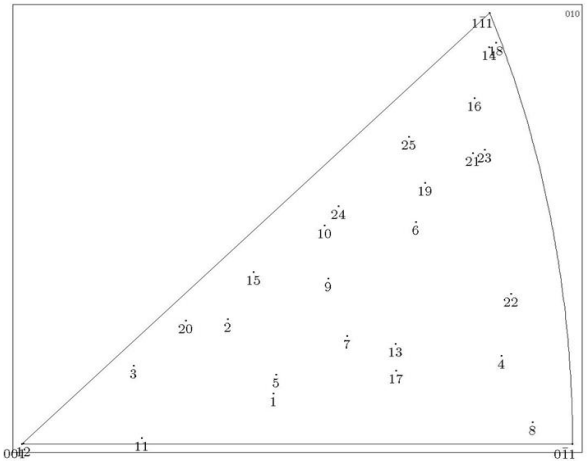

Fig. 12 The inverse pole Fig. of the loading direction, which is the y-axis of the global coordinate, generated by a MATLAB toolbox code called MTEX developed by Hielscher et al. [53].

There are several material constants relating to the constitutive equations of elasto-plastic behaviour of a single crystal. They were obtained by the following procedure:

(a) Literature results: Elastic moduli in the reduced form of elastic moduli tensor [54], the critical annihilation distance y_c [55] and the dislocation interaction matrix [56]. The shear modulus is given by $G = \sqrt{(C_{11} - C_{12}) \times C_{44}/2}$ [31].

(b) Experimental results: Average grain size D_{grain} from SEM, the initial dislocation density ρ_0 from TEM and Burger's vector b from XRD.

(c) Inverse Method: Other parameters, arranged in an array $\boldsymbol{q} = [C, D, \dot{\gamma}_0, n\ K]$ were obtained by iteratively approximating the volume averaged stress-strain results of the illustrative model from FE simulations to the experimental results, obtained from the stabilised cyclic response at a strain range of $\pm 0.4\%$ between cycle number 800 and 1500. The optimisation process is available in the toolbox of MATLAB by the function **lsqcurvefit**, to find an array of unknown material constants $\boldsymbol{q}$ that fit a series of experimental data $(xdata, ydata)$. It is conducted by minimising the difference between the FE simulation results $F(q, xdata)$ and objective values *ydata*, based on a nonlinear least-squares algorithm.

Since no units were required when providing material constants in ABAQUS, the unit system with length defined in *mm*, force defined in *N*, mass defined in *tonne* was chosen for the whole model. Therefore, in the result output file, stress would be presented as *MPa*, and energy would be presented as *mJ*. The material constants obtained for the single crystal constitutive equations are summarized in Table 4.

The hysteresis loops obtained by FE simulation after the inverse method and by the 1000th cycle of the fatigue specimen at a strain range of $\pm 0.2\%$. The difference in the slope of the elastic region is caused by the elastic anisotropy of the single crystals, and this kind of difference principally can be reduced by increasing the grain number of the illustrative model. In addition, the transition of the elastic to plastic region of the FE result is less smooth than the experimental result.

Table 4. Material Constants defined in the UMAT subroutine

C_{11}(MPa)	C_{12}(MPa)	C_{44}(MPa)	C	D	$\dot{\gamma}_0$ (s^{-1})	n	ρ_0 (mm^{-2})	D_{grain}
204600	126200	137700	36000	600	1.00E-04	50	1e8	0.05
b (mm)	y_c (mm)	K	a_0	a_1	a_2	a_3	a_4	a_5
2.534E-07	7.50E-05	3.55	0.0454	0.625	0.0454	0.0454	0.137	0.122

4.3 Convergence Study

As pointed out in Section 2.2, it is generally agreed that 10^3 to 10^4 numbers of grains of random orientations are recommended to ensure that the grain number is large enough to represent the macroscopic behaviour of a material containing the order of billions of grains statistically. In addition, smaller element sizes and thus more integration points are favoured to allow for large intragranular deformation. However, considering computational efficiency and the limitation in computational power, a convergence study is necessary to minimise the grain number and integration points.

In order to evaluate the convergence behaviour of the macroscale stress and strain output regardless of the grain orientations and the element size, tensile tests were simulated on the 25-grain model by applying a displacement loading at Face 1 at a strain of 2%.

The orientation convergence study was conducted by assigning another two sets of random grain orientations (Orientations No.2 and 3) to the 25-grain model, in addition to the grain orientation set in Fig. 12 (Orientation No.1). The element size was 3.8, which divides the sizes of the geometry into 20 equal segements. The average stress-strain behaviour in the y-direction for the tensile tests is shown in Fig. 13. The stress responses in the elastic region based on three sets of grain orientations follows roughly the same path. When the material behaviour enters the plastic deformation, the largest stress difference based on different orientations was less than 10%.

The element size convergence study was conducted by assigning three element sizes of 1.9, 3.8 and 7.6 to the geometry, which divides the sizes of the geometry into 40, 20 and 10 equal segements separately. The grain orientations of the 25 grains were the same as Orientation No.1. The stress responses in the elastic region based on three element sizes follows roughly the same path. When the material behaviour enters the plastic deformation, the stress difference between element sizes 7.6 and 3.8 is less than 4%, while the stress difference between element sizes 3.8 and 1.9 is less than 1%.

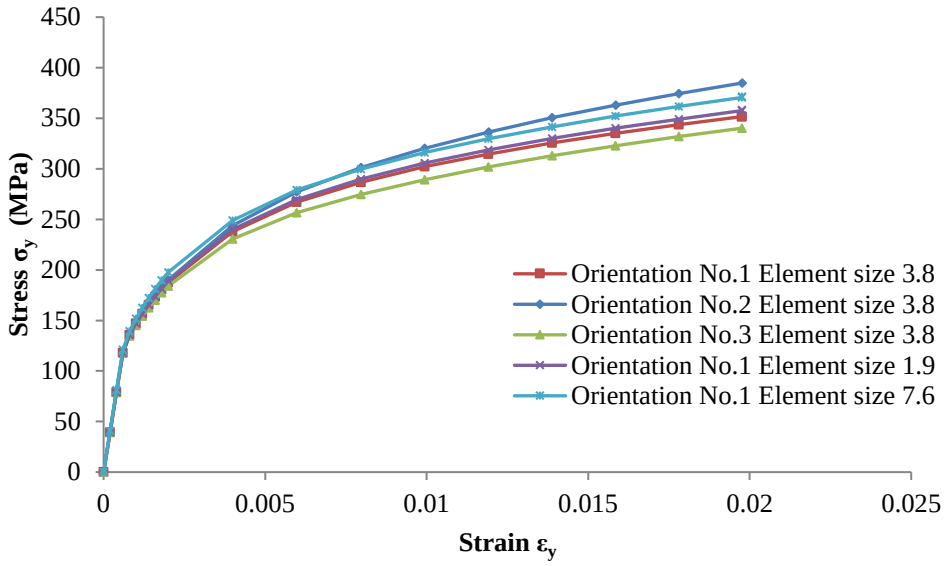

Fig. 13 Stress-strain curve for the tensile test with various orientations

Since the analysis was constrained in the small deformation range, a cyclic displacement loading within the strain range $\pm 0.2\%$ at a strain rate of $4 \times 10^{-3} s^{-1}$ in the y-direction was applied at Face 1. The average stress-strain hysteresis loops for the fatigue tests based on three sets of grain orientations are shown in Fig. 14. The maximum difference between the results is less than 5%. Negligible differences are observed for the hysteresis loops simulated using element sizes 3.8 and 1.9.

Therefore, the 25 grain geometry and the element size of 3.8 was considered to be sufficient to approximate the RVE under this specified loading condition for the first few cycles, when there is minor plastic deformation. They are used to investigate the local variable distribution in the following FE analysis.

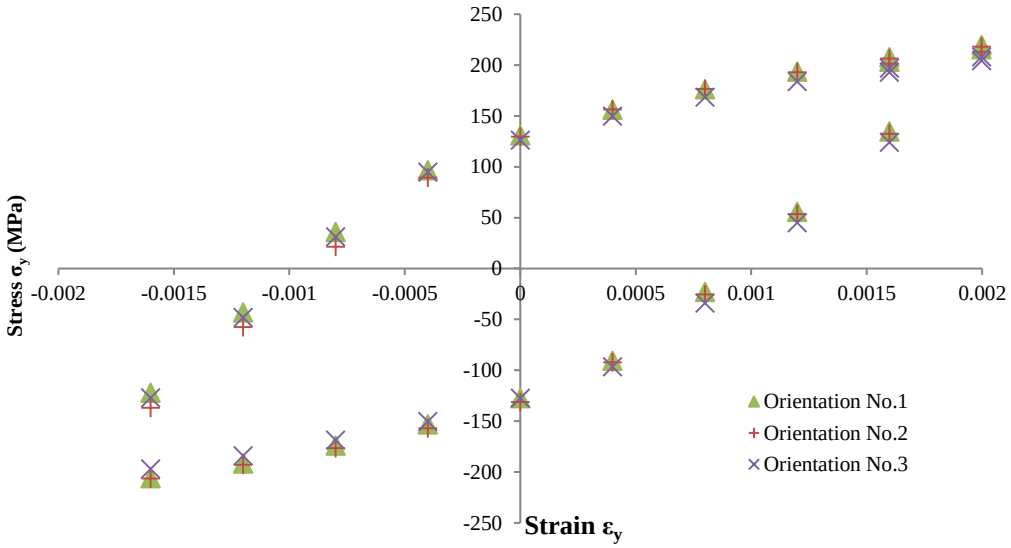

Fig. 14 Stress-Strain curve for the fatigue test with various orientations

4.4 Preliminary results

After numerical stabilisation at the third cycle when the displacement loading reaches the maximum value, the highly heterogeneous distribution of the maximum principal stress and strain are plotted in Figs. 15 and 16. The difference of the strain deformation and stress response between grains is mainly caused by the difference in the grain orientation, whereas the difference inside a grain is mainly caused by the grain arrangements and their interactions. The highly

anisotropic elastic and plastic behaviour of a single crystal causes the deformation or stress concentration of the grain boundaries to satisfy both the stress equilibrium and strain compatibility. Therefore, both stress and strain concentration tend to occur at grain boundaries.

For example, the results of soft grains, such as Grains 9 and 17 is usually a combination of higher than average strain deformation 0.4% and lower than average stress response; whereas the results of hard grains such as Grains 14 and 18 are a combination of lower than average strain deformation and higher than average stress response. The hysteresis loops obtained from soft grain 9 and hard grain 14 are shown in Fig. 17, which shows clearly the elastic anisotropy and plastic anisotropy between the hard grain and soft grain. Compared with the bulk behaviour, Grain 9 has a lower apparent Young's modulus, yield stress and overall stress response, but larger plastic deformation and higher hysteresis energy; In contrast, the loading direction of Grain 14 located near the vertices $[1\bar{1}1]$ of the inverse pole figure., has a higher apparent Young's modulus and yield stress, due to more numbers of slip systems being activated.

In the case of Grain 12, whose loading directions are located near the vertice [001], it exhibits larger than average strain deformation in part of the grain, and about average stress response seem from the hysteresis loop plotted in Fig. 17. Observed from the standard stereographic projection, eight slip systems, including C3, D4, A2, C1, B4, A3, D1 and B2, are located among the vertices. These slip systems are activated simultaneously during the fatigue test at the same rate.

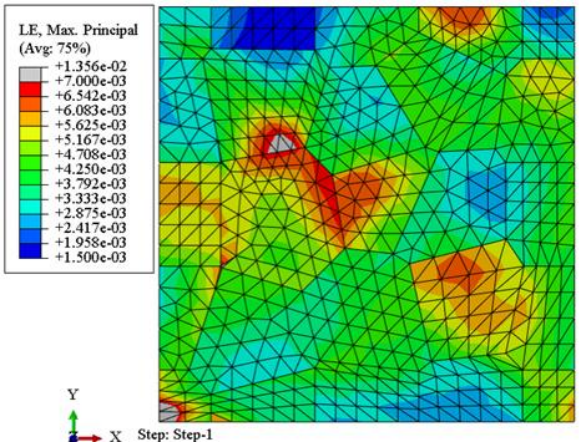

Fig. 15 Maximum principal stress distribution

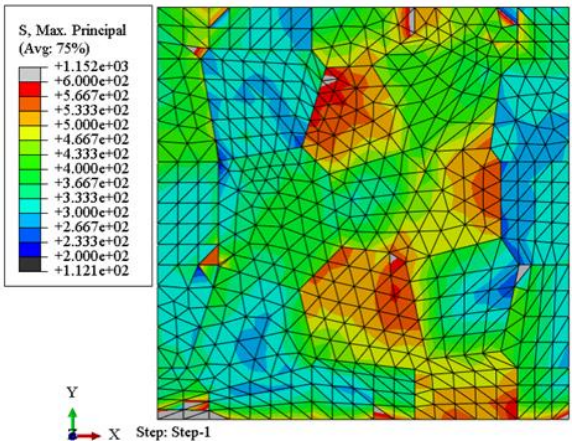

Fig. 16 Maximum principal stress distribution

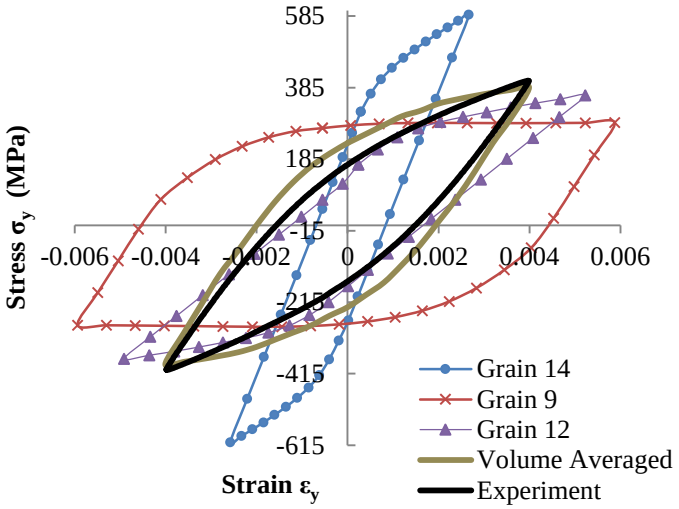

Fig. 17 Local and volume-averaged stress-strain curves in the y-direction showing the grain orientation and interaction effects

Fig. 18 shows the dislocation densities distribution for the slip system C5 $(11\bar{1})[1\bar{1}0]$ (SDV121 in ABAQUS, representing solution dependent variable 121), and it shows that Grains 8, 14, and 18 were activated completely, while Grains 9 and 13 were partially activated in part of the grains. The reason behind this phenomena can be demonstrated via the inverse pole figure, since the standard triangle enclosing C5 shares the trace of plane (011), which is the edge linking vertices $[1\bar{1}1]$ and $[0\bar{1}1]$. Therefore, Grains 8, 14 and 18 located near the trace of plane (011) would activate once the load is applied. Due to grain interaction, even if Grains 9 and 13 are not orientated favourably to the slip system C5, it is still partially activated. In addition, similar to stress and strain concentration sites, dislocations also tend to pile up at grain boundaries.

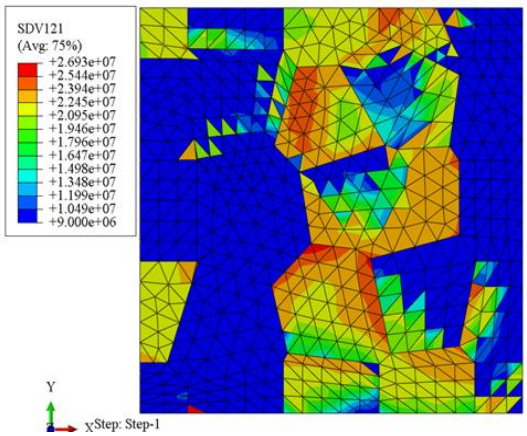

Fig. 18 Dislocation density of the slip system C5 $(11\bar{1})[1\bar{1}0]$ (*SDV121* in UMAT subroutine).

The distributions of the crack initiation indicators, including accumulated plastic deformation and plastic hysteresis energy, were defined in the UMAT as SDV133 and ELPD, as shown in Figs. 19 and 20. The contour distribution of the accumulated plastic strain appears to be similar to the principal strain distribution, and both indicate that Grains 9, 13 and 17 are possible microcrack initiation sites. However, the prediction of microcrack initiation sites based on the plastic dissipation energy is stricter than the accumulated plastic strain criterion, which indicates that Grains 9 and 13 are possible microcrack initiation sites. Plastic dissipation energy considers both the stress and strain history. However, the accuracy and validity of each crack initiation indicator needs further experimental investigation.

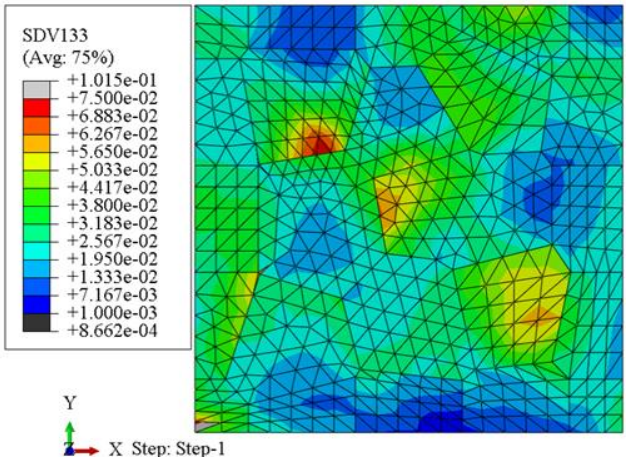

(a) (b)

Fig. 19 The distributions of microcrack initiation indicators: (a) accumulated plastic deformation (*SDV133* in the UMAT subroutine) ;

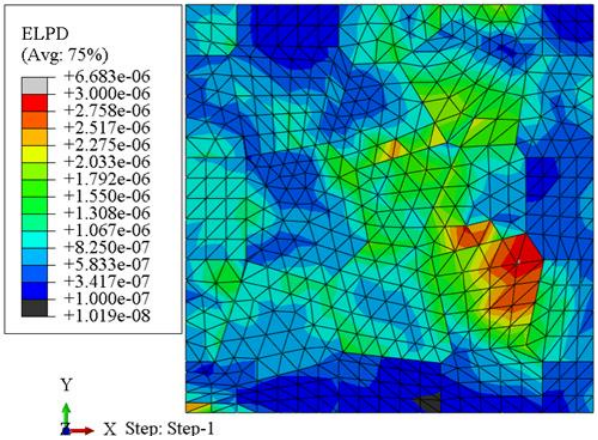

Fig. 20 local plastic dissipation energy (*ELPD* in ABAQUS).

5. Discussion and Conclusion

Since fatigue failure is closely related to microstructure, the CPFEM approach was incorporated into the commercially available software ABAQUS by coding a UMAT user subroutine and some Python post-processors. This method is used mainly to investigate the effect of grain orientation on the local stress and strain distribution in this paper.

A series of experimental investigations, including SEM, TEM and XRD, were conducted for the as-received material in order to understand the cyclic plasticity behaviour and to establish a methodology to determine some of the material constants in the single crystal constitutive equations in CPFEM. The average grain size was determined from SEM, and Burger's vector was determined from XRD. The initial dislocation density was determined by TEM, though from a limited region instead of being obtained on an average basis. The elastic moduli, shear modulus and material constants related to the dislocation interaction were obtained from the literature. The other five material constants in the flow rule, kinematic hardening evolution and dislocation evolution rule were obtained by an inverse method. Although this method cannot guarantee a unique set of material constants, it is still applicable to investigate the local stress and strain distributions.

The fractured surface gives an indication that the specimen is fractured by the initial fatigue damage, with the level and bright surfaces showing fatigue striations. With the development of fatigue damage and the effect of local stress concentration, the specimen failed by ductile fracture with a dimpled surface. In addition, sulphide, including MnS, FeS and CrS, act as crack initiation sites. The significance of the precipitate in the crack initiation prediction has not been considered in the current study, but will be included in future work.

From the CPFEM results, the constitutive equations proposed were shown to be able to predict the local stress and

strain distribution based on the given grain orientations and arrangements. Several conclusions can be summarized from the CPFEM results. Firstly, there is a large intragranular and intergranular heterogeneity, since the local behaviour is determined by grain orientation, as well as the grain interaction. Secondly, as observed from the results of stress and strain distributions, the grain boundary plays a vital role in satisfying stress equilibrium and strain compatibility. Thirdly, the CPFEM framework used in this paper can be used to predict the crack initiation sites based on the local accumulated plastic deformation and local plastic dissipation energy criterion, but limited when applied to the precipitate effect.

References

1. Dunne, F.P.E., A.J. Wilkinson, and R. Allen, *Experimental and computational studies of low cycle fatigue crack nucleation in a polycrystal.* International Journal of Plasticity, 2007. **23**(2): p. 273-295.

2. Bhat, S.P. and M.E. Fine, *Fatigue crack nucleation in iron and a high strength low alloy steel.* Materials Science and Engineering: A, 2001. **314**(1–2): p. 90-96.

3. Hanlon, T., Y.N. Kwon, and S. Suresh, *Grain size effects on the fatigue response of nanocrystalline metals.* Scripta Materialia, 2003. **49**(7): p. 675-680.

4. Hanlon, T., E.D. Tabachnikova, and S. Suresh, *Fatigue behavior of nanocrystalline metals and alloys.* International Journal of Fatigue, 2005. **27**(10–12): p. 1147-1158.

5. Davidson, D.L., R.G. Tryon, M. Oja, R. Matthews, and K.S. Ravi Chandran, *Fatigue Crack Initiation In WASPALOY at 20 °C.* Metallurgical and Materials Transactions A, 2007. **38**(13): p. 2214-2225.

6. Oja, M., K.S. Ravi Chandran, and R.G. Tryon, *Orientation Imaging Microscopy of fatigue crack formation in Waspaloy: Crystallographic conditions for crack nucleation.* International Journal of Fatigue, 2010. **32**(3): p. 551-556.

7. Taylor, G.I., *Plastic strain in metals.* Journal Institute of Metals, 1938. **62**: p. 307-324.

8. Kubin, L., B. Devincre, and T. Hoc, *Modeling dislocation storage rates and mean free paths in face-centered cubic crystals.* Acta Materialia, 2008. **56**(20): p. 6040-6049.

9. Devincre, B. and L. Kubin, *Scale transitions in crystal plasticity by dislocation dynamics simulations.* Comptes Rendus Physique, 2010. **11**(3–4): p. 274-284.

10. Fine, M.E. and S.P. Bhat, *A model of fatigue crack nucleation in single crystal iron and copper.* Materials Science and Engineering: A, 2007. **468–470**(0): p. 64-69.

11. Voothaluru, R. and C.R. Liu, *A crystal plasticity based methodology for fatigue crack initiation life prediction in polycrystalline copper.* Fatigue & Fracture of Engineering Materials & Structures, 2014: p. n/a-n/a.

12. Tanaka, K. and T. Mura, *A Dislocation Model for Fatigue Crack Initiation.* Journal of Applied Mechanics, 1981. **48**(1): p. 97-103.

13. Brückner-Foit, A. and X. Huang, *Numerical simulation of micro-crack initiation of martensitic steel under fatigue loading.* International Journal of Fatigue, 2006. **28**(9): p. 963-971.

14. Glodež, S., M. Šori, and J. Kramberger, *A statistical evaluation of micro-crack initiation in thermally cut structural elements.* Fatigue & Fracture of Engineering Materials & Structures, 2013. **36**(12): p. 1298-1305.

15. Manonukul, A. and F.P.E. Dunne, *High– and low–cycle fatigue crack initiation using polycrystal plasticity.* Proceedings of the Royal Society of London. Series A: Mathematical, Physical and Engineering Sciences, 2004. **460**(2047): p. 1881-1903.

16. Cheong, K.-S., M.J. Smillie, and D.M. Knowles, *Predicting fatigue crack initiation through image-based micromechanical modeling.* Acta Materialia, 2007. **55**(5): p. 1757-1768.

17. Bieler, T.R., P. Eisenlohr, F. Roters, D. Kumar, D.E. Mason, M.A. Crimp, and D. Raabe, *The role of heterogeneous deformation on damage nucleation at grain boundaries in single phase metals.* International Journal of Plasticity, 2009. **25**(9): p. 1655-1683.

18. Le Pécheur, A., F. Curtit, M. Clavel, J.M. Stephan, C. Rey, and P. Bompard, *Polycrystal modelling of fatigue: Pre-hardening and surface roughness effects on damage initiation for 304L stainless steel.* International Journal of Fatigue, 2012. **45**(0): p. 48-60.

19. Feaugas, X. and P. Pilvin, *A Polycrystalline Approach to the Cyclic Behaviour of f.c.c. Alloys – Intra-Granular Heterogeneity.* Advanced Engineering Materials, 2009. **11**(9): p. 703-709.

20. Li, Y., V. Aubin, C. Rey, and P. Bompard, *The effects of variable stress amplitude on cyclic plasticity and microcrack initiation in austenitic steel 304L.* Computational Materials Science, 2012. **64**(0): p. 7-11.

21. Li, Y., V. Aubin, C. Rey, and P. Bompard, *Polycrystalline numerical simulation of variable amplitude loading effects on cyclic plasticity and microcrack initiation in austenitic steel 304L.* International Journal of Fatigue, 2012. **42**(0): p. 71-81.

22. Schwartz, J., O. Fandeur, and C. Rey, *Numerical approach of cyclic behaviour of 316LN stainless steel based on a polycrystal modelling including strain gradients.* International Journal of Fatigue, 2013. **55**(0): p. 202-212.

23. Guilhem, Y., S. Basseville, F. Curtit, J.M. Stéphan, and G. Cailletaud, *Investigation of the effect of grain clusters on fatigue crack initiation in polycrystals.* International Journal of Fatigue, 2010. **32**(11): p. 1748-1763.

24. Guilhem, Y., S. Basseville, F. Curtit, J.-M. Stéphan, and G. Cailletaud, *Numerical investigations of the free surface effect in three-dimensional polycrystalline aggregates.* Computational Materials Science, 2013. **70**(0): p. 150-162.

25. Sweeney, C.A., W. Vorster, S.B. Leen, E. Sakurada, P.E. McHugh, and F.P.E. Dunne, *The role of elastic anisotropy, length scale and crystallographic slip in fatigue crack nucleation.* Journal of the Mechanics and Physics of Solids, 2013. **61**(5): p. 1224-1240.

26. Chang, H.-J., *Analysis of Nano indentation Size effect based on Dislocation Dynamics and Crystal Plasticity, PhD Thesis*. 2009, L'Institut polytechnique de Grenoble et de Seoul National University: France.

27. Asaro, R.J. and V.A. Lubarda, *Mechanics of solids and materials* 2006: Cambridge University Press.

28. Asaro, R.J., *Crystal plasticity.* Journal of Applied Mechanics, 1983. **50**(4b): p. 921-934.

29. Roters, F., P. Eisenlohr, L. Hantcherli, D.D. Tjahjanto, T.R. Bieler, and D. Raabe, *Overview of constitutive laws, kinematics, homogenization and multiscale methods in crystal plasticity finite-element modeling: Theory, experiments, applications.* Acta Materialia, 2010. **58**(4): p. 1152-1211.

30. Erieau, P. and C. Rey, *Modeling of deformation and rotation bands and of deformation induced grain boundaries in IF steel aggregate during large plane strain compression.* International Journal of Plasticity, 2004. **20**(10): p. 1763-1788.

31. Harder, J., *A crystallographic model for the study of local deformation processes in polycrystals.* International Journal of Plasticity, 1999. **15**(6): p. 605-624.

32. Bassani, J.L. and T.-Y. Wu, *Latent Hardening in Single Crystals II. Analytical Characterization and Predictions.* Proceedings of the Royal Society of London. Series A: Mathematical and Physical Sciences, 1991. **435**(1893): p. 21-41.

33. Van Houtte, P., S. Li, M. Seefeldt, and L. Delannay, *Deformation texture prediction: from the Taylor model to the advanced Lamel model.* International Journal of Plasticity, 2005. **21**(3): p. 589-624.

34. Kröner, E., *Zur plastischen verformung des vielkristalls.* Acta Metallurgica, 1961. **9**(2): p. 155-161.

35. Becker, R., *Analysis of texture evolution in channel die compression—I. Effects of grain interaction.* Acta Metallurgica et Materialia, 1991. **39**(6): p. 1211-1230.

36. Diard, O., S. Leclercq, G. Rousselier, and G. Cailletaud, *Evaluation of finite element based analysis of 3D multicrystalline aggregates plasticity: Application to crystal plasticity model identification and the study of stress and strain fields near grain boundaries.* International Journal of Plasticity, 2005. **21**(4): p. 691-722.

37. Barbe, F., L. Decker, D. Jeulin, and G. Cailletaud, *Intergranular and intragranular behavior of polycrystalline aggregates. Part 1: F.E. model.* International Journal of Plasticity, 2001. **17**(4): p. 513-536.

38. Aalco. *Stainless steel-austenitic-1.4301 Bar and Section*. 2015 04/09/2015]; Available from: http://www.aalco.co.uk/datasheets/Stainless-Steel-14301-Bar-and-Section_34.ashx.

39. *British Standard: Metallic materials-Fatigue testing-Strain-controlled thermomechanical fatigue testing method: BS ISO 12111:2011(E)*. 2011, BSI Standards Publication: UK.

40. Feltner, C.E. and C. Laird, *Cyclic stress-strain response of F.C.C. metals and alloys—II Dislocation structures and mechanisms.* Acta Metallurgica, 1967. **15**(10): p. 1633-1653.

41. Mughrabi, H., F. Ackermann, and K. Herz, *Persistent Slipbands in fatigued face-centered and body-centered cubic metals*, in *Fatigue Mechanics*, J.T. Fong, Editor. 1979, ASTM International.

42. Davis, J.R., *Stainless steels*. 1994: ASM international.

43. Räty, R., V. Lindroos, A. Saarinen, J. Forstén, and H.M. Miekk-Oja, *The preparation of thin foils for electron microscopy using a controlled low temperature technique.* Journal of Scientific Instruments, 1966. **43**(6): p. 367.

44. Norfleet, D.M., D.M. Dimiduk, S.J. Polasik, M.D. Uchic, and M.J. Mills, *Dislocation structures and their relationship to strength in deformed nickel microcrystals.* Acta Materialia, 2008. **56**(13): p. 2988-3001.

45. Brandon, D. and W.D. Kaplan, *Microstructural Characterization of Materials*. 2nd ed. 2008, UK: John Wiley & Sons, Ltd.

46. Kalidindi, S.R., C.A. Bronkhorst, and L. Anand, *Crystallographic texture evolution in bulk deformation processing of FCC metals.* Journal of the Mechanics and Physics of Solids, 1992. **40**(3): p. 537-569.

47. Sarma, G. and T. Zacharia, *Integration algorithm for modeling the elasto-viscoplastic response of polycrystalline materials.* Journal of the Mechanics and Physics of Solids, 1999. **47**: p. 1219-1238.

48. Dumoulin, S., O.S. Hopperstad, and T. Berstad, *Investigation of integration algorithms for rate-dependent crystal plasticity using explicit finite element codes.* Computational Materials Science, 2009. **46**(4): p. 785-799.

49. Asaro, R.J. and A. Needleman, *Overview no. 42 Texture development and strain hardening in rate dependent polycrystals.* Acta Metallurgica, 1985. **33**(6): p. 923-953.

50. Huang, Y., *A user-material subroutine incorporating single crystal plasticity in the ABAQUS finite element program*, in *Division of applied sciences*. 1991, Harvard University.

51. Peirce, D., C.F. Shih, and A. Needleman, *A tangent modulus method for rate dependent solids.* Computers & Structures, 1984. **18**(5): p. 875-887.

52. Quey, R., P.R. Dawson, and F. Barbe, *Large-scale 3D random polycrystals for the finite element method: Generation, meshing and remeshing.* Computer Methods in Applied Mechanics and Engineering, 2011. **200**(17–20): p. 1729-1745.

53. Bachmann, F., R. Hielscher, and H. Schaeben, *Texture analysis with MTEX–free and open source software toolbox.* Solid State Phenomena, 2010. **160**: p. 63-68.

54. Vitos, L., P.A. Korzhavyi, and B. Johansson, *Stainless steel optimization from quantum mechanical calculations.* Nat Mater, 2003. **2**(1): p. 25-28.

55. Cleveringa, H.H.M., E. Van der Giessen, and A. Needleman, *A discrete dislocation analysis of mode I crack growth.* Journal of the Mechanics and Physics of Solids, 2000. **48**(6–7): p. 1133-1157.

56. Devincre, B., L. Kubin, and T. Hoc, *Physical analyses of crystal plasticity by DD simulations.* Scripta Materialia, 2006. **54**(5): p. 741-746.

Appendix A. Expression of the Rotational Matrix

The local coordinate specified by the slips direction $\boldsymbol{m}^{\alpha}$ and normal directions $\boldsymbol{n}^{\alpha}$ could be transformed interchangeably by the 3D rotational matrix $\boldsymbol{R_3}$ to the the global coordinate specified by the slips direction $\boldsymbol{m}^{*\alpha}$ and normal directions $\boldsymbol{n}^{*\boldsymbol{\alpha}}$, for the α^{th} slip system, as follows:

$$\boldsymbol{m}^{*\alpha} = \boldsymbol{R_3} \cdot \boldsymbol{m}^{\alpha} \;\; and \;\; \boldsymbol{n}^{*\boldsymbol{\alpha}} = \boldsymbol{R_3} \cdot \boldsymbol{n}^{\alpha} \tag{A.1}$$

The rotational matrix is determined by grain orientation, which is commonly expressed by Euler angles $(\varphi_1, \Phi, \varphi_2)$, and the 3D rotational matrix $\boldsymbol{R_3}$ is formulated as follows:

$$\boldsymbol{R_3} = \begin{pmatrix} cos(\varphi_1)\, cos(\varphi_2) - sin(\varphi_1)\, sin(\varphi_2)\, cos(\Phi) & -\cos(\varphi_1)\sin(\varphi_2) - \sin(\varphi_1)\cos(\varphi_2)\cos(\Phi) & \sin(\varphi_1)\sin(\Phi) \\ sin(\varphi_1)\cos(\varphi_2) + \cos(\varphi_1)\sin(\varphi_2)\cos(\Phi) & -\sin(\varphi_1)\sin(\varphi_2) + \cos(\varphi_1)\cos(\varphi_2)\cos(\Phi) & -\cos(\varphi_1)\sin(\Phi) \\ \sin(\varphi_2)\sin(\Phi) & \cos(\varphi_2)\sin(\Phi) & \cos(\Phi) \end{pmatrix} \tag{A.2}$$

In the FE software ABAQUS, the stress tensor is presented as an array $(\sigma_{11}, \sigma_{22}, \sigma_{33}, \sigma_{12}, \sigma_{13}, \sigma_{23})$ for numerical efficiency, and similar to the strain tensor. Therefore, the 4th order elasticity moduli tensor $\boldsymbol{\mathcal{L}}$ is reduced to a 6×6 matrix**.** For cubic crystals, the elasticity moduli matrix in the local coordinate $\boldsymbol{C}$ is governed by three independent variables C_{11}, C_{12} and C_{44}, as follows:

$$\boldsymbol{C} = \begin{pmatrix} C_{11} & C_{12} & C_{12} & 0 & 0 & 0 \\ C_{12} & C_{11} & C_{12} & 0 & 0 & 0 \\ C_{12} & C_{12} & C_{11} & 0 & 0 & 0 \\ 0 & 0 & 0 & C_{44} & 0 & 0 \\ 0 & 0 & 0 & 0 & C_{44} & 0 \\ 0 & 0 & 0 & 0 & 0 & C_{44} \end{pmatrix} \tag{A.3}$$

A six-dimensional rotational matrix $\boldsymbol{R_6}$ transforms the elasticity moduli matrix from the local coordinate $\boldsymbol{C}$ to the global coordinate $\boldsymbol{C_{global}}$ as follows:

$$\boldsymbol{C_{global}} = \boldsymbol{R_6 C R_6^{-1}} \tag{A.4}$$

and

$$\boldsymbol{R}_6 = \begin{pmatrix} {R_{11}}^2 & {R_{12}}^2 & {R_{13}}^2 & 2R_{12}R_{13} & 2R_{11}R_{13} & 2R_{11}R_{12} \\ {R_{21}}^2 & {R_{22}}^2 & {R_{23}}^2 & 2R_{22}R_{23} & 2R_{21}R_{23} & 2R_{21}R_{22} \\ {R_{31}}^2 & {R_{32}}^2 & {R_{33}}^2 & 2R_{32}R_{33} & 2R_{31}R_{33} & 2R_{31}R_{32} \\ R_{21}R_{31} & R_{22}R_{32} & R_{23}R_{33} & R_{22}R_{33} + R_{32}R_{23} & R_{21}R_{33} + R_{31}R_{23} & R_{21}R_{32} + R_{22}R_{31} \\ R_{11}R_{31} & R_{12}R_{32} & R_{13}R_{33} & R_{12}R_{33} + R_{32}R_{13} & R_{11}R_{33} + R_{31}R_{13} & R_{11}R_{32} + R_{31}R_{12} \\ R_{21}R_{11} & R_{12}R_{22} & R_{13}R_{23} & R_{12}R_{23} + R_{22}R_{13} & R_{11}R_{23} + R_{21}R_{13} & R_{11}R_{22} + R_{21}R_{12} \end{pmatrix} \tag{A.5}$$

where R_{ij} are entries of the rotational matrix $\boldsymbol{R_3}$ in the i^{th} row and j^{th} column.

Appendix B. Flowchart of the CPFEM model